

Ligand-induced reaction mechanism regulation on Sr/Nb₂O₅ for high-efficiency selective photocatalytic NO oxidation

Tianjiao Wu^a, Bibo Ma^a, Huanhuan Bai^a, Lin Wang^a, Yumei Zhang^a, Qingzhi Luo^a, Jing An^a, Huiying Mu^a, Desong Wang^{a,b,*}, Yandong Duan^{a,**}

^a Hebei Key Laboratory of Photoelectric Control on Surface and Interface, School of Sciences, Hebei University of Science and Technology, Shijiazhuang 050018, People's Republic of China

^b State Key Laboratory of Metastable Materials Science and Technology (MMST), Hebei Key Laboratory of Applied Chemistry, Yanshan University, Qinhuangdao 066004, People's Republic of China

ARTICLE INFO

Keywords:
Photocatalysis
NO deep oxidation
Nb₂O₅
Strontium
Reaction mechanism

ABSTRACT

Developing highly efficient photocatalysts that selectively convert NO pollutants to NO₃⁻ while storing metabolic nitrogen for crops remains a great challenge. Simultaneously, there is a dearth of research investigating the relationship between the chemical environment and the activity of catalytic sites. Herein, an efficient impregnation approach to access atomically dispersed Sr single atoms supported on Nb₂O₅ is reported; meanwhile, various ligands (-Cl, -Br, -OH) are employed to customize the local structure. The results show that Cl-Sr/Nb₂O₅ exhibits excellent catalytic performance in eliminating NO, which is significantly superior to other catalysts. The introduction of Sr atom and ligand increases the energy barrier of NO₂ formation, thus improving the selectivity of converting NO to NO₃⁻. This study highlights the importance of precisely designing the catalytic site at the atomic level, and the obtained insights may serve as a valuable guide for developing future catalyst designs.

1. Introduction

The nitric oxide (NO) concentration in the atmosphere has drastically increased over the past few decades due to the development of industries and the growth of automobiles. NO is an atmospheric pollutant with detrimental effects on the environment, including the generation of photochemical smog, acid rain, and depletion of the ozone layer [1–3]. Therefore, scavenging NO is critical to maintaining the ecological balance and is an urgent concern. Several techniques have been employed to decrease oxynitride emissions; nevertheless, conventional physical or chemical adsorption and thermal catalytic reduction approaches are impractical for eliminating NO at a ppb level [4–8]. Since Honda and Fujishima et al. discovered photocatalysis in 1972, semiconductor photocatalysis technology has attracted much attention due to the characteristics of being sustainable, economical, and no secondary pollution, and is considered to be a promising solution to environmental problems [9]. Graphite phase carbon nitride (g-C₃N₄), titanium dioxide-related materials, and bismuth-based materials have

been extensively researched for the purpose of photocatalytic oxidation to eliminate NO [2,10–17]. NO₂ is a common adverse product in the photocatalytic process, and its toxicity is 8.48 times that of NO [18]. How to efficiently promote the deep oxidation of NO to NO₃⁻ (NO₃⁻ can be used as a storage form of metabolic nitrogen in crops) while inhibiting the production of hazardous intermediates NO₂ has become the research hotspot.

Metal oxide-supported single atom catalysts (SACs), which were first proposed by Zhang and colleagues more than a decade ago, have received increasing attention in the chemical industry due to their advantages of highly uniform and well-defined active centers and high atomic utilization [19]. Oxide supports are abundant and versatile, and their local structure can be easily modified, enabling more considerable flexibility for optimizing the catalytic activity via tailoring the electronic metal-support interaction (EMSI) [20–24]. Metal oxides, particularly high-valence metal oxides (e.g., Nb₂O₅), display stronger EMSI than other options (e.g., carbon and metals) since their oxygen atoms are more likely to interact with the d states of metal atoms [25–29]. At the

* Corresponding author at: Hebei Key Laboratory of Photoelectric Control on Surface and Interface, School of Sciences, Hebei University of Science and Technology, Shijiazhuang 050018, People's Republic of China.

** Corresponding author.

E-mail addresses: dswang06@126.com (D. Wang), yduan@iccas.ac.cn (Y. Duan).



same time, the coordinating environment of SACs also have a crucial impact on the activity and selectivity of SACs. The accessibility to regulate the coordination of SACs may result in intriguingly catalytic characteristics [30–33]. However, systematic investigations into optimizing photocatalytic oxidation activity via controllable modifications of the chemical environment around atomically dispersed catalytic sites are rare.

In this work, we aim to enhance the photocatalytic capability of NO elimination by implementing a wetness impregnation method to anchor atomically dispersed Sr single-sites onto the Nb_2O_5 support. Additionally, we can further customize the Sr-sites using various strontium salts to achieve modification with different ligands. The obtained Sr/ Nb_2O_5 exhibits a remarkably improved catalytic performance in the process of NO deep oxidation, and ligands play a crucial role in improving photocatalytic activity and selectivity. The present study offers a simple and economical approach for fabricating efficient photocatalysts to eliminate NO.

2. Experimental section

2.1. Materials

Strontium chloride hexahydrate ($\text{SrCl}_2 \cdot 6 \text{ H}_2\text{O}$) was acquired from Aladdin Biochemical Technology Co., LTD (Shanghai, China). Macklin Biochemical Technology Co., LTD (Shanghai, China) provided strontium bromide hexahydrate ($\text{SrBr}_2 \cdot 6 \text{ H}_2\text{O}$) and strontium hydroxide ($\text{Sr}(\text{OH})_2 \cdot 8 \text{ H}_2\text{O}$). Hydrochloric acid (HCl) was supplied by Tianjin Kermel Chemical Reagent Co., LTD (Tianjin, China). Ashinecarbon Co., Ltd. provided the niobium pentoxide (Nb_2O_5).

2.2. Preparation of photocatalysts

Synthesis of Cl-Sr/ Nb_2O_5 : $\text{SrCl}_2 \cdot 6 \text{ H}_2\text{O}$ (0.0410 mg) was dissolved in 1 mM HCl (12.5 mL). After being stirred for 2 h, an appropriate amount of Nb_2O_5 was added to the above solution under stirring, and the solution was continuously stirred for 5 h at room temperature. Afterward, the mixture was stirred at 90 °C for 3 h until the solvent was evaporated. The sample was then loaded into a muffle furnace and calcined at 450 °C in the air for 2 h to obtain Cl-Sr/ Nb_2O_5 .

Synthesis of Br-Sr/ Nb_2O_5 : $\text{SrBr}_2 \cdot 6 \text{ H}_2\text{O}$ (0.0548 mg) was dissolved in 12.5 mL of deionized water. The following steps are the same as for the preparation of Cl-Sr/ Nb_2O_5 .

Synthesis of OH-Sr/ Nb_2O_5 : OH-Sr/ Nb_2O_5 was prepared by the same method as that Br-Sr/ Nb_2O_5 except that 0.0408 mg $\text{Sr}(\text{OH})_2 \cdot 8 \text{ H}_2\text{O}$ was used to substitute $\text{SrBr}_2 \cdot 6 \text{ H}_2\text{O}$ in the first step.

2.3. Characterization

The morphology of the samples was examined by scanning electron microscopy (SEM, TESCAN MIRA LMS, Czech Republic) and the spherical aberration-corrected transmission electron microscope (AC-TEM, Thermo Fisher Titan Themis G2 60–300). X-ray diffraction (XRD) patterns were conducted on a powder diffractometer (D/max 2500PC, Rigaku), using Cu-K α radiation as X-ray source ($\lambda = 0.15406 \text{ nm}$, 40 kV, 150 mA). The UV-2550 ultraviolet-visible spectrometer (Shimadzu, Japan) was used to record the diffuse reflectance spectroscopy. Thermo scientific K-Alpha instrument with 72 W Al K α X-rays was used to conduct X-ray photoelectron spectroscopy (XPS). The binding energies were calibrated by contaminant C at 284.8 eV. The photoluminescence (PL) spectrum was acquired on F-4600 (Tokyo, Japan) under 325 nm laser irradiation. The Sr contents in the samples were analyzed by inductively coupled plasma mass spectrometry (ICP-MS, Agilent 5110). A Bruker EMXplus-6/1 spectrometer was used to conduct electron paramagnetic resonance (EPR) measurements. Samples for EPR measurement were prepared by mixing the samples in a 50 mM DMPO solution (aqueous dispersion for DMPO-•OH and methanol dispersion for

DMPO-• O_2^-). The analysis of Sr K-edge was conducted on the BL14W1 beamlines at the Shanghai Synchrotron Radiation Facility (SSRF) (Shanghai, China), using Si (111) crystal as a monochromator. The X-ray absorption fine structure (XAFS) spectra were captured using a 4-channel Silicon Drift Detector (SDD) Bruker 5040. Sr K-edge extended X-ray absorption fine structure (EXAFS) spectra were recorded in transmission mode. The spectra were processed and analyzed by the software codes Athena and Artemis.

2.4. XANES simulations

The simulations utilized the FDMNES software, which employs the finite difference method (FDM) to solve the Schrödinger equation and incorporates the Green formalism. During the simulations, the final states were determined within a spherical region centered on the Sr atoms. The radius of the sphere was set to 6 Å, and only the atoms located within the sphere were taken into account [34].

2.5. Photocatalytic and photoelectrochemical performance

The photocatalytic performance was evaluated in a continuous-flow chamber under simulated sunlight (Xenon lamp). The initial concentration of NO was diluted to 500 ppb by controlling the air flow (2.4 L min $^{-1}$) and NO flow (15 mL min $^{-1}$). The catalyst (200 mg) was evenly coated on the glass plate and then placed in the flow reactor. The simulated solar light source shines vertically on the photocatalyst through the quartz window of reactor. A NO-NO $_2$ -NO $_x$ analyzer (42i-TL, THERMO FISHER, American) was used to continuously detect and measure NO concentrations at 1 min intervals. The remove rate (η) of NO was calculated using the following equation: $\eta = 1 - (c/c_0) \times 100\%$, where c is the actual NO concentration in ppb and c_0 is the inflow concentration (about 500 ppb) after reaching adsorption-desorption equilibrium. The electrochemical characteristics of the photocatalysts were evaluated in a three-electrode system utilizing CHI 660E electrochemical workstation, and 0.2 mol L $^{-1}$ Na $_2\text{SO}_4$ aqueous solution was used as electrolyte. The working electrode was prepared by coating the photocatalyst on ITO glass. Pt wire was used as counter electrode and an Ag/AgCl electrode was employed as the reference electrode.

2.6. Theoretical calculation method

Vienna ab initio Simulation Package (VASP) was used to perform all calculations based on density functional theory (DFT) [35–37]. To describe the exchange-correlation potentials and electron-electron interactions, the Perdew–Burke–Ernzerhof (PBE) exchange-correlation density functional, along with the generalized gradient approximation, was employed [38]. The kinetic cut-off energy was set at 400 eV. Energy (EDIFF) and force (EDIFFG) convergence criteria were set to 1.0×10^{-5} eV and $-0.05 \text{ eV}/\text{\AA}$, respectively. A vacuum spacing was set as at least 15 Å. A (1 × 1 × 1) Monkhorst-Pack grids of k-points was used to sample the Brillouin zone integration. The calculation of adsorption energy (E_{ads}) was performed as:

$$E_{\text{ads}} = E_{\text{adsorbate/catalyst}} - E_{\text{adsorbate}} - E_{\text{catalyst}} \quad (1)$$

where $E_{\text{adsorbate/catalyst}}$, $E_{\text{adsorbate}}$, and E_{catalyst} are the total energies of the molecule adsorbed on the catalyst, the isolated gas molecules, and pure catalyst, respectively. The Gibbs free energy changes (ΔG) were calculated to investigate the NO oxidation pathway, and ΔG is calculated as: $\Delta G = \Delta E + \Delta E_{\text{ZPE}} - T\Delta S$, where ΔE represents the change of reaction energy, ΔE_{ZPE} represents the change of zero-point energy, T is the temperature (298.15 K), and ΔS is the change in entropy.

2.7. In-situ DRIFTS

In-situ DRIFTS measurements were performed using Bruker

INVENIOR FT-IR spectrometer equipped with in-situ diffuse reflectance cell (Harrick). Prior to the adsorption procedure, the cell was purged with high-purity He for 1 h at 150 °C to clean the photocatalyst surface and the baseline was collected after cooling to room temperature. Afterward, the mixture of NO (15 mL min⁻¹) and O₂ (30 mL min⁻¹) was introduced into the reaction chamber. The mixture was adsorbed on the surface of the photocatalyst for 20 min in the dark and then the reactor was irradiated for 30 min with a 300 W Xe lamp.

3. Results and discussion

3.1. The morphology and structural characterization

Fig. 1a and S1a-b depict the morphology of pure Nb₂O₅ nanorods, exhibiting a length ranging from 200 to 400 nm and a diameter ranging from 50 to 150 nm. XRD patterns were measured to investigate the crystal structures of the catalysts (**Fig. 1b**). Obviously, diffraction peaks at around 16.97, 22.61, 28.31, 36.50, 45.00, 46.06, 50.89, and 54.97° can be, respectively, indexed to (130), (001), (180), (181), (330), (002), (380), and (182), which assigned to an orthorhombic phase of Nb₂O₅ (T-phase, JCPDS card no. 27–1003) [39]. The XRD patterns of Cl-Sr/Nb₂O₅, Br-Sr/Nb₂O₅, and OH-Sr/Nb₂O₅ exhibit comparable peaks attributed to

Nb₂O₅ and do not present any peaks corresponding to metallic or oxide Sr species. A possible explanation is that the Sr species exhibit uniform distribution on the surface of Nb₂O₅. Alternatively, this phenomenon could also be attributed to only a minimal amount of Sr loaded on the Nb₂O₅ surface, resulting in undetectable signals [40]. The Sr loading content of samples was determined by ICP analysis as ca. 1.0 wt% (**Table S1**). The surface loading of strontium salt has no obvious effect on the specific surface area of Nb₂O₅ (**Fig. S2** and **Table S2**). We further investigated the sample by spherical aberration-corrected electron microscope (**Fig. 1c** and S3). Since the atomic number of Sr (Z = 38) is only slightly lower than that of Nb (Z = 41), it is difficult to distinguish the Sr atoms in terms of contrast. The AC-TEM image obtained from Cl-Sr/Nb₂O₅ exhibits a lattice fringe with an interplanar spacing of 0.39 nm. This interplanar distance is associated with the lattice spacing of the (001) crystal facet of orthorhombic Nb₂O₅. The surface chemical compositions of the Cl-Sr/Nb₂O₅, Br-Sr/Nb₂O₅, and OH-Sr/Nb₂O₅ were studied by elemental mapping characterization. **Fig. 1d** and S3c-f show a uniform distribution of Nb, Sr, O, and Cl/Br elements. The coordination environment and electronic structure of Sr sites on Cl-Sr/Nb₂O₅, Br-Sr/Nb₂O₅, and OH-Sr/Nb₂O₅ were analyzed using X-ray absorption near-edge structure (XANES and EXAFS) spectroscopies. The XANES spectra of the aforementioned samples demonstrate a near-edge

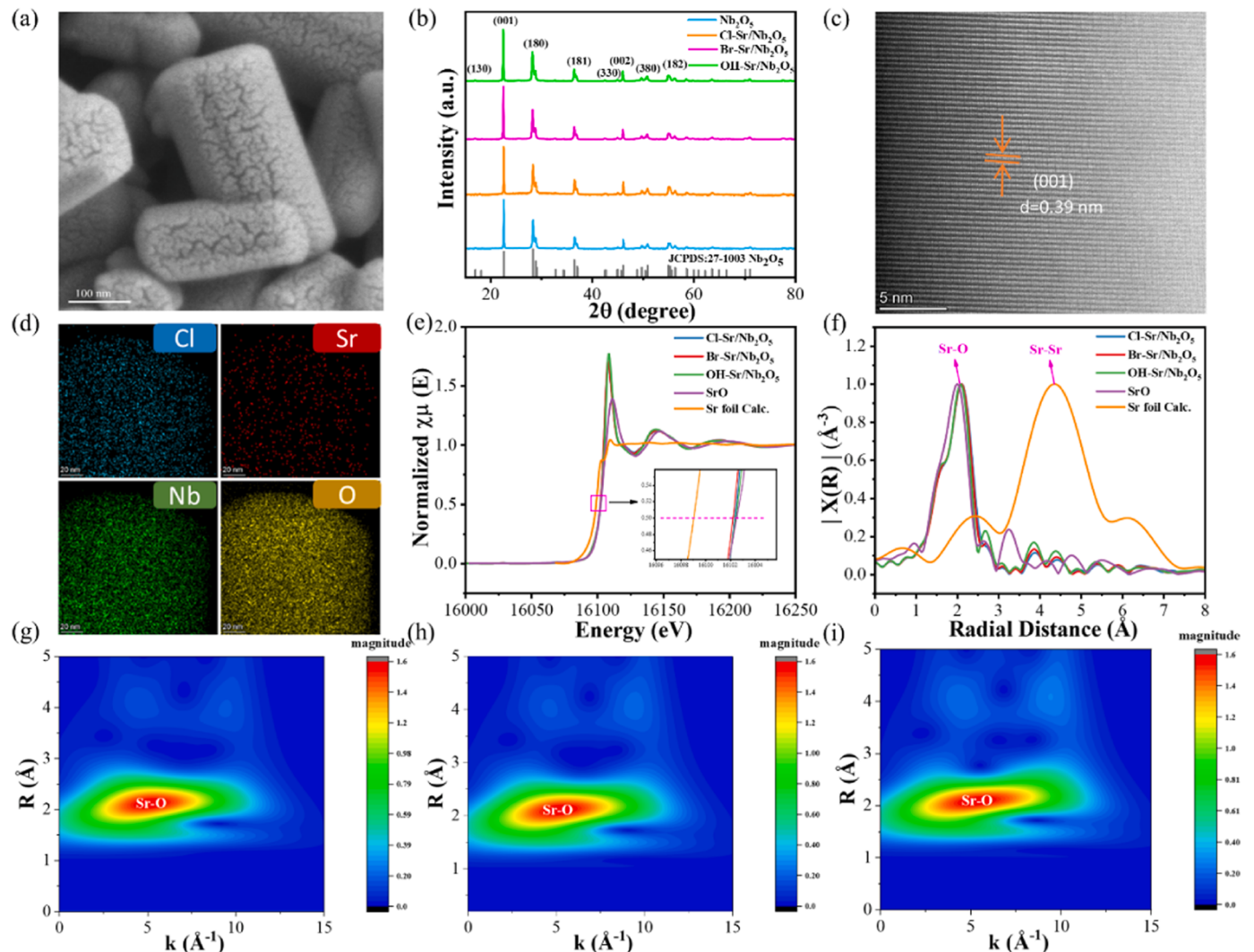


Fig. 1. (a) SEM image of Nb₂O₅. (b) The XRD patterns of Nb₂O₅, Cl-Sr/Nb₂O₅, Br-Sr/Nb₂O₅, and OH-Sr/Nb₂O₅. (c)-(d) The high-angle annular dark-field scanning TEM (HAADF-STEM) images of Cl-Sr/Nb₂O₅ and the corresponding EDX mappings of Cl, Sr, Nb, and O. (e) The Sr K-edge XANES spectra. (f) The Sr K-edge FT-EXAFS. (g)-(i) The wavelet transforms of the Cl-Sr/Nb₂O₅, Br-Sr/Nb₂O₅, and OH-Sr/Nb₂O₅. Acquiring Sr foil for XAFS testing is challenging due to its high instability. Through computational simulation, we acquired XANES and FT-EXAFS spectra of a Sr metal.

configuration that is similar to.

the reference compound SrO. This similarity implies that the average oxidation state of Sr in Cl-Sr/Nb₂O₅, Br-Sr/Nb₂O₅, and OH-Sr/Nb₂O₅ is around 2 (Fig. 1e). As shown in Fourier-transform (FT) EXAFS spectra, compared to the SrO, the other samples display only one major peak at 2.1 Å, attributed to Sr-O coordination. No peak at 4.2 Å associated with Sr-Sr coordination is detected, demonstrating the Sr species in samples exists as Sr-O bond without any Sr-Sr aggregation (Fig. 1f). The EXAFS data-fitting results (Fig. S4 and Table S3) show that the Sr-O coordination number is approximately 4 in Cl-Sr/Nb₂O₅ and Br-Sr/Nb₂O₅, and the number is approximately 5 in OH-Sr/Nb₂O₅. The Sr atom can only coordinate with up to three oxygen on the Nb₂O₅ (001) crystal plane, and since it is difficult to distinguish Sr-O bonds from Sr-Cl/Br bonds by EXAFS, the extra coordination number is contributed by Cl/Br elements and O elements of OH ligand. In the theoretical calculation section, we build the structural model of the material on this basis. Moreover, the wave vector (k) is crucial in differentiating various coordination atoms surrounding Sr. The strong oscillation seen in the samples' k space mostly manifests in the low k region. This observation implies that the coordination of Sr is predominantly facilitated by atoms with smaller atomic numbers, such as O, Cl, or Br, rather than Sr atoms themselves. EXAFS wavelets transform in Fig. 1g-i and S5 also confirms the above results.

3.2. The surface chemical state and charge distribution

The surface chemical state of the catalysts was analyzed by XPS, and the XPS fine spectra of Sr 3d, Nb 3d, O 1 s, Cl 2p and Br 3d are shown in

Fig. 2a-c and S6a-b. Furthermore, the surface atoms were examined using Bader charge analysis. Fig. 2d presents the optimized structure of Nb₂O₅, Cl-Sr/Nb₂O₅, Br-Sr/Nb₂O₅, and OH-Sr/Nb₂O₅, and the calculated atomic Bader charge is summarized in Table S4. The deconvoluted spectrum of Sr 3d exhibits a pair of peaks at 133.5–133.6 eV and 135.2–135.3 eV, revealing the 3d_{5/2} and 3d_{3/2} with an interval of 1.7 eV (Fig. 2a), indicating that the oxidation number of Sr atom is about 2 [41, 42]. Compared to Cl-Sr/Nb₂O₅ and Br-Sr/Nb₂O₅, the Sr 3d peak of OH-Sr/Nb₂O₅ has higher binding energy, meaning that the Sr ions can have higher chemical valence. Fig. 2d reveals that the Bader charge of interfacial Sr1 (blue spheres) is calculated to be 8.418, 8.425, and 8.373 on Cl-Sr/Nb₂O₅, Br-Sr/Nb₂O₅, and OH-Sr/Nb₂O₅ respectively, indicating Sr lose more electrons in the OH-Sr/Nb₂O₅, which well accords with the result of XPS. Moreover, as shown in Fig. 2b, noticeable differences are observed in Nb 3d spectrum when Sr is loaded on the surface of Nb₂O₅, and the peaks corresponding to Nb 3d_{3/2} and 3d_{5/2} exhibit a negative shift of ca. 0.3 eV, suggesting increased electron density in Nb₂O₅ [43]. The Cl-Sr/Nb₂O₅ and Br-Sr/Nb₂O₅ exhibit a distinct shift to lower binding energies compared to that of OH-Sr/Nb₂O₅. These shifts were

ascribed to the interaction of the Nb atoms with Sr species. The Bader charge of interfacial Nb2 (green spheres) are 10.477, 10.547, 10.548, and 10.467 on Nb₂O₅, Cl-Sr/Nb₂O₅, Br-Sr/Nb₂O₅,

and OH-Sr/Nb₂O₅ respectively, indicating stronger Nb-O bonding in the OH-Sr/Nb₂O₅. As for O 1 s (Fig. 2c), the samples exhibit two distinct peaks at 530.1 and 531.8 eV, corresponding to the presence of lattice oxygen (O_L) in Nb₂O₅ and a hydroxyl group (-OH), respectively. In comparison to OH-Sr/Nb₂O₅, the O 1 s binding energy of Cl-Sr/Nb₂O₅

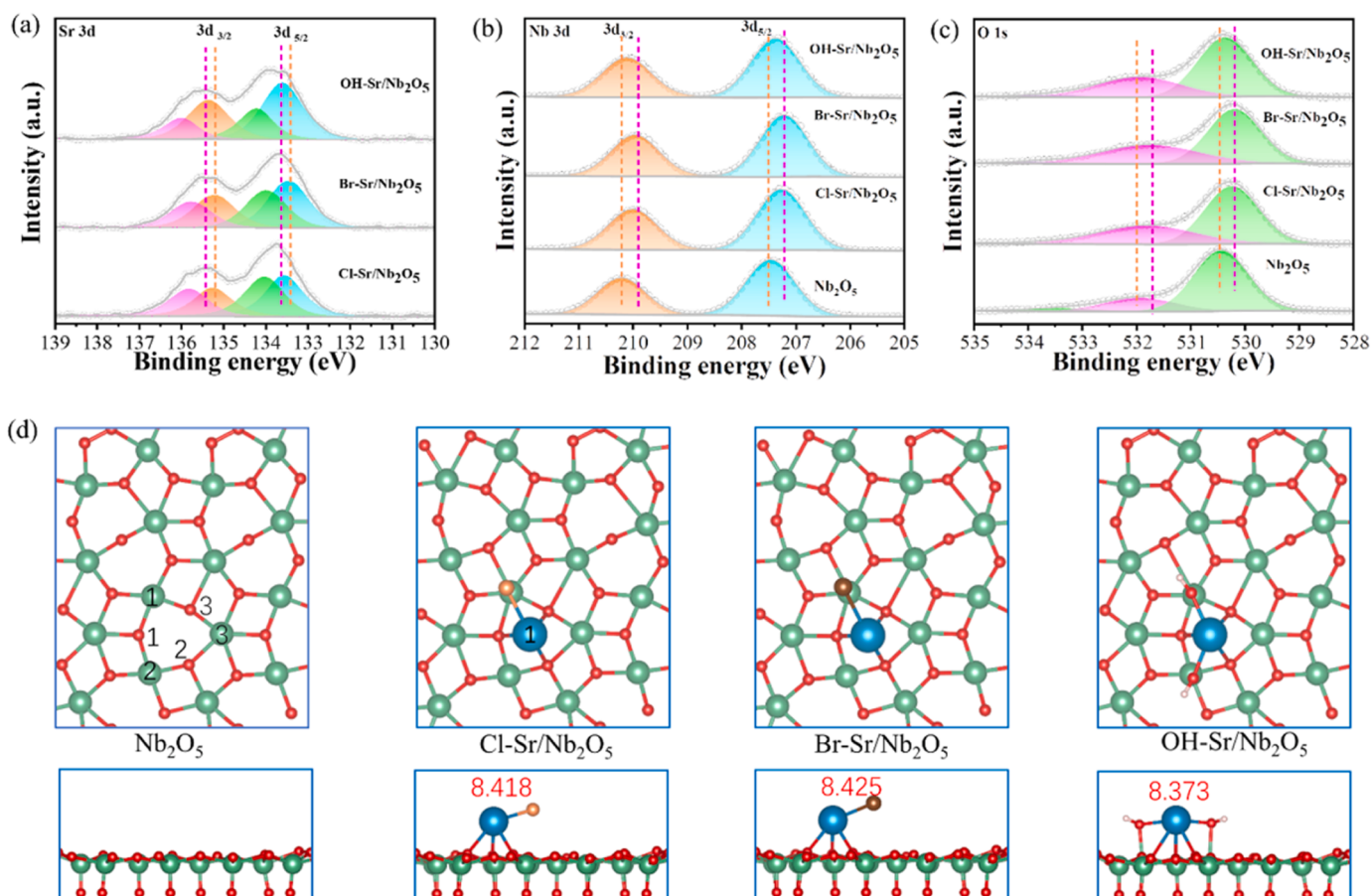


Fig. 2. XPS spectra of Sr 3d (a), Nb 3d (b) and O 1 s (c) of Nb₂O₅, Cl-Sr/Nb₂O₅, Br-Sr/Nb₂O₅, and OH-Sr/Nb₂O₅. (d) Structural model and Bader charge analysis typical atoms of Nb₂O₅, Cl-Sr/Nb₂O₅, Br-Sr/Nb₂O₅, and OH-Sr/Nb₂O₅. The red, green, blue, orange, brown, and pink spheres represent Nb, O, Sr, Cl, Br, and H atoms, respectively.

and Br-Sr/Nb₂O₅ display a negative shift of 0.23 eV and 0.3 eV, respectively. This further confirmed the efficient electron transfer between Sr atoms and Nb₂O₅. Significantly, Cl 2p peaks (199.5 and 198.0 eV) and Br 3d peaks (69.3 and 68.3 eV) were detected in Cl-Sr/Nb₂O₅ and Br-Sr/Nb₂O₅. These observed peaks closely correspond to the binding energies associated with Cl 2p in Cl⁻ and Br 3d in Br⁻, respectively (Fig. S6a-b) [44]. These differences in XPS binding energy and Bader charge confirmed that the electronic structures of Nb₂O₅ can be altered through charge redistribution. Both experimental and theoretical analysis suggest the significance of various ligands (-Cl, -Br, -OH) in altering the charge density and electronic structure of Sr atoms through charge redistribution, which would further affect their catalytic performance.

The side and top views of the differential charge density for the Cl-Sr/Nb₂O₅, Br-Sr/Nb₂O₅, and OH-Sr/Nb₂O₅ structure are shown in Fig. 3a-c and S7. The evident charge redistributions at the Sr-O bonding

region suggest significant interaction between the Nb₂O₅ and Sr atom. Moreover, the distances between Sr atom and Nb₂O₅ layer are 1.98 Å, 1.96 Å, and 2.23 Å for Cl-Sr/Nb₂O₅, Br-Sr/Nb₂O₅, and OH-Sr/Nb₂O₅. To obtain a quantitative evaluation of the charge transfer, the planar-average charge density difference along the z-axis is calculated by integrating the electron density differences, as depicted in Fig. 3d-f. In this case, regions of charge accumulation (yellow area) are highlighted by positive values of $\Delta\rho(z)$, whereas regions of charge depletion (cyan area) are marked by negative values of $\Delta\rho(z)$. The calculated values

for charge transfer value are 0.470 e⁻, 0.590 e⁻, and 0.228 e⁻ for Cl-Sr/Nb₂O₅, Br-Sr/Nb₂O₅, and OH-Sr/Nb₂O₅. The redistribution of the charge density would induce an interfacial built-in electric field, extending from the Nb₂O₅ plane to the protruding Sr atom at the interface [45–47]. To obtain a more profound understanding of the inherent built-in electric field, we have generated a graphical representation of the vertical-direction plane-averaged electrostatic potential

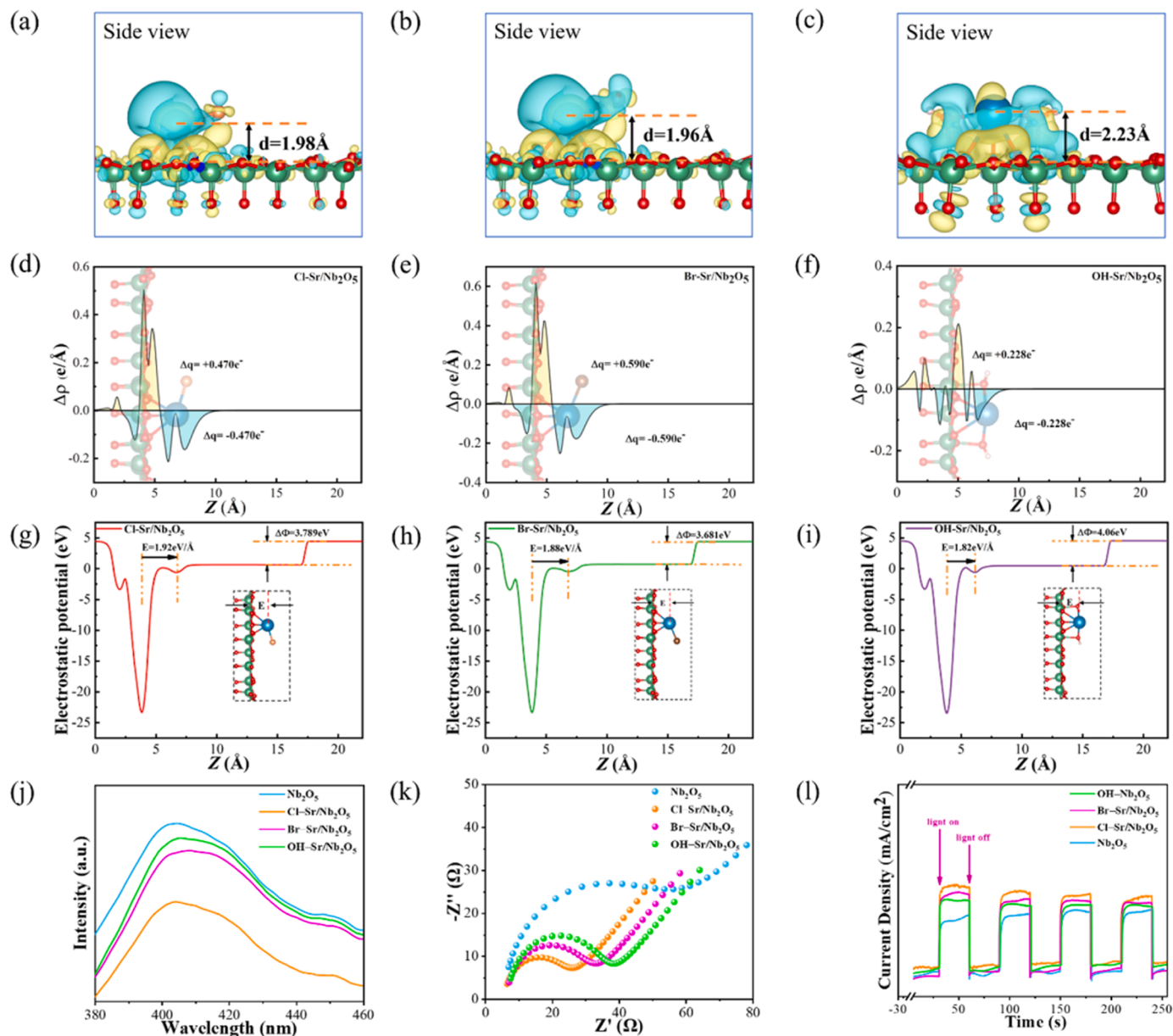


Fig. 3. (a)-(c) The differential charge density of Cl-Sr/Nb₂O₅, Br-Sr/Nb₂O₅, and OH-Sr/Nb₂O₅ (yellow refers to charge accumulation and cyan refers to charge loss). (d)-(f) Planar-averaged electron density difference for Cl-Sr/Nb₂O₅, Br-Sr/Nb₂O₅, and OH-Sr/Nb₂O₅. $\Delta\Phi$ is the potential energy difference. (j) PL spectra of Nb₂O₅, Cl-Sr/Nb₂O₅, Br-Sr/Nb₂O₅ and OH-Sr/Nb₂O₅. (k) EIS Nyquist of Nb₂O₅, Cl-Sr/Nb₂O₅, Br-Sr/Nb₂O₅, and OH-Sr/Nb₂O₅. (l) Transient photocurrent density responses of Nb₂O₅, Cl-Sr/Nb₂O₅, Br-Sr/Nb₂O₅, and OH-Sr/Nb₂O₅.

distribution, as illustrated in Fig. 3g-i. The electric field can be quantitatively expressed as: $E = \Delta\Phi/d$ [48,49], and E of Cl-Sr/Nb₂O₅, Br-Sr/Nb₂O₅, and OH-Sr/Nb₂O₅ is calculated to be 1.92, 1.88, and 1.82 eV/Å, respectively. This built-in electric field could accelerate the separation efficiency of photogenerated electrons and holes.

The PL spectra of Nb₂O₅, Cl-Sr/Nb₂O₅, Br-Sr/Nb₂O₅, and OH-Sr/Nb₂O₅ are displayed in Fig. 3j, and pure Nb₂O₅ exhibits the maximum PL intensity. The introduction of Sr atoms results in a significant drop in PL intensity. Compared with Nb₂O₅, Br-Sr/Nb₂O₅ and OH-Sr/Nb₂O₅, Cl-Sr/Nb₂O₅ has the lowest strength, indicating that charge recombination is inhibited and has the highest charge separation efficiency. Furthermore, the photocurrent EIS test is conducted to analyze the electron transport and recombination. As shown in the Nyquist.

plots (Fig. 3k), among all the samples, Cl-Sr/Nb₂O₅ shows the smallest radius of the semicircle. This observation indicates a low charge transfer resistance and a high efficiency in separating carriers. Fig. 3l illustrates the spectra of photocurrent response, revealing that Cl-Sr/Nb₂O₅ featured higher photocurrents than Br-Sr/Nb₂O₅, OH-Sr/Nb₂O₅ and Nb₂O₅. This result further verifies the efficient transfer of charges and the effective separation of electrons holes in the Cl-Sr/Nb₂O₅ material.

3.3. Photocatalytic performance and mechanism

The formation of reactive oxygen species (ROS) has considerable significance in surface photochemical processes. Three crucial prerequisites for the production of reactive oxygen species (ROS) are the adsorption of O₂ and H₂O, the formation of photoinduced charge carriers, and the activation of reactants. Consequently, an examination of the adsorption and activation of H₂O and O₂ molecules on the surface of the samples was conducted using DFT simulations. (Fig. 4a-h and S8-9).

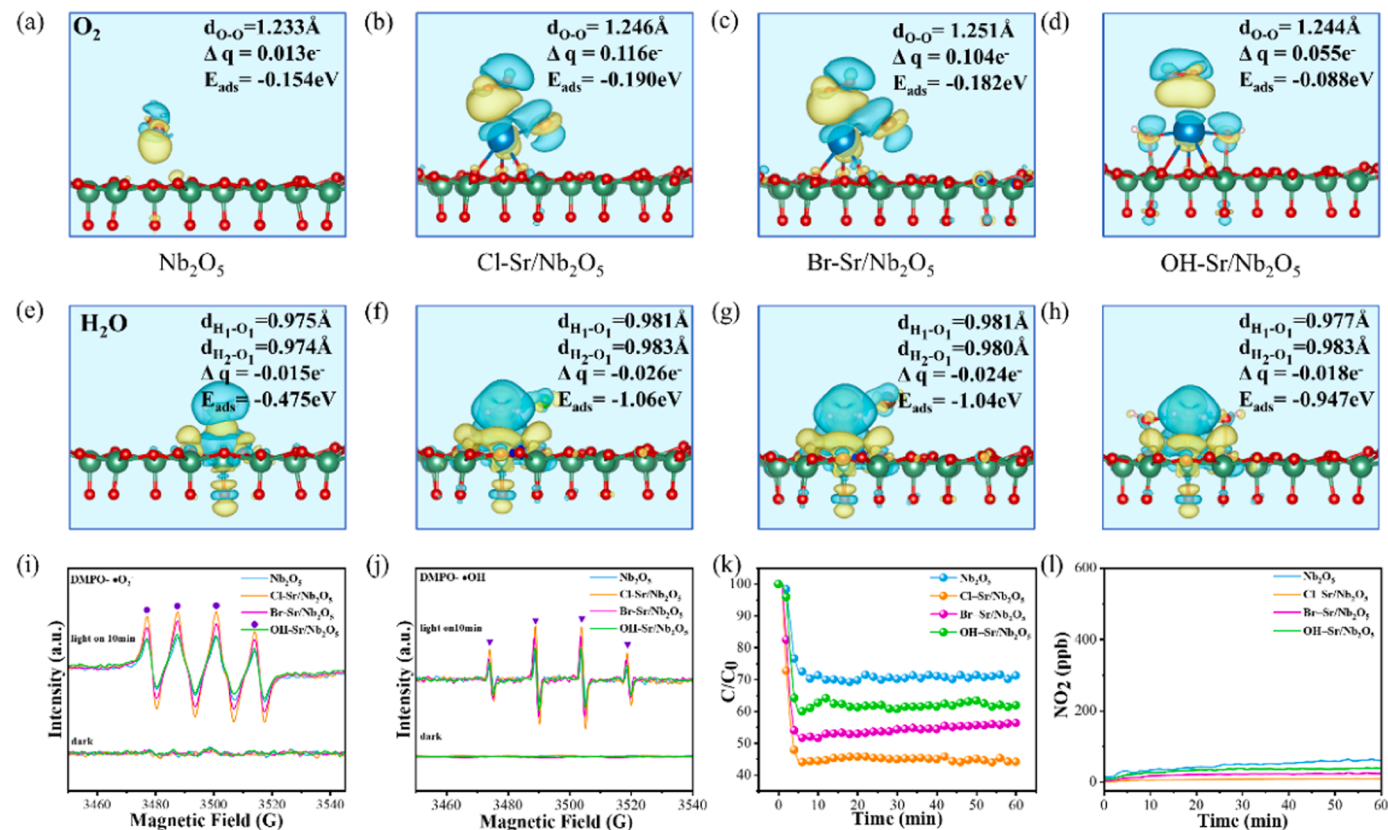


Fig. 4. Charge differences for optimized O₂ (a)-(d) and H₂O (e)-(h) adsorption structure on the surface of Nb₂O₅, Cl-Sr/Nb₂O₅, Br-Sr/Nb₂O₅, and OH-Sr/Nb₂O₅ (side view). Yellow area: electron accumulation; Cyan area: electron depletion. (i)-(j) DMPO spin-trapping •O₂⁻ and •OH EPR spectra of Nb₂O₅, Cl-Sr/Nb₂O₅, Br-Sr/Nb₂O₅, and OH-Sr/Nb₂O₅. (k) Photocatalytic performance of Nb₂O₅, Cl-Sr/Nb₂O₅, Br-Sr/Nb₂O₅ and OH-Sr/Nb₂O₅ for NO oxidation. (l) The amount of NO₂ generated.

The O₂ adsorption energy on the surface of Nb₂O₅ is determined to be -0.154 eV, while the O-O bond length of O₂ is measured to be 1.233 Å. By comparing the adsorption capacity of O₂ on different sample surfaces (Fig. 4a-d and S8), the results show the supported Sr single atoms with Cl/Br (except OH-Sr/Nb₂O₅) increase the adsorption energy for O₂ and enhance the electron transfer from the samples to O₂. Notably, Cl-Sr/Nb₂O₅ exhibits the highest adsorption energy among the studied samples ($E_{ads} = -0.190$ eV). The electron transfer channels formed between Sr and Nb₂O₅ make it easier for electrons to reach the surface, and thus exhibit stronger activation of O₂. This enhanced activation promotes the generation of superoxide free radicals ($\bullet\text{O}_2^-$) and facilitates subsequent surface photocatalytic reactions.

The hydroxyl radical is a crucial component in the complete oxidation process of NO. The adsorption and activation of H₂O on the sample surface were modelled using DFT calculations, as shown in Fig. 4e-h and S9. The adsorption energies of H₂O on Cl-Sr/Nb₂O₅, Br-Sr/Nb₂O₅ and OH-Sr/Nb₂O₅ are -1.06 eV, -1.04 eV and -0.947 eV, respectively, which are much higher than -0.475 eV of Nb₂O₅ and the H-O bond length of H₂O is also elongated. The above calculations demonstrate that the introducing Sr single atoms on Nb₂O₅ may enhance the adsorption and activation of O₂ and H₂O, and facilitate the formation of $\bullet\text{O}_2^-$ and $\bullet\text{OH}$ radicals.

The presence of reactive oxygen species (ROS) was confirmed by electron paramagnetic resonance spectroscopy characterization. As depicted in Fig. 4i-j, there are no apparent $\bullet\text{O}_2^-$ and $\bullet\text{OH}$ signals for the samples in the dark; nevertheless, with the visible light excitation, the samples of Nb₂O₅, Cl-Sr/Nb₂O₅, Br-Sr/Nb₂O₅ and OH-Sr/Nb₂O₅ exhibit four characteristic peaks of the $\bullet\text{OH}$ and $\bullet\text{O}_2^-$, at the range of 3480–3540 G (magnetic field strength) [50–52]. The $\bullet\text{O}_2^-$ and $\bullet\text{OH}$ signals are significantly enhanced when the samples are exposed to visible light, and the strongest radical signals appear when exposing the

Cl-Sr/Nb₂O₅ to light. The increased intensity of •O₂⁻ and •OH signals may be ascribed to the greater adsorption and activation of O₂ and H₂O molecules, as well as the accelerated spatial charge separation. Fig. 4k demonstrates the improved catalytic performance of Nb₂O₅ catalysts after introducing Sr single atoms. The catalysts exhibit NO conversion with 28.26% for Nb₂O₅, 57.01% for Cl-Sr/Nb₂O₅, 49.76% for Br-Sr/Nb₂O₅, 39.76% for OH-Sr/Nb₂O₅, respectively, which probably evidencing that anions have a critical impact on the catalytic behavior of metal oxides. In addition, as shown in Fig. 4l, the amount of harmful intermediate NO₂ released over Cl-Sr/Nb₂O₅ is also the lowest of all catalysts. The level of NO₂ emission, which is less than 10 ppb, falls below the primary and secondary National Ambient Air Quality Standards of NO₂ set by the Environmental Protection Agency (EPA-456/F-99-006a, 53 ppb) [53].

In the context of extended durations exceeding 6 h, the photocatalytic elimination of NO was effectively carried out using Cl-Sr/Nb₂O₅, as seen in Fig. 5a-b. This catalyst exhibited commendable durability in the repeated removal of NO at a concentration of 500 ppb, while demonstrating little decline in activity and insignificant emission of NO₂. In order to determine the ratio of NO₂⁻ / NO₃⁻ in the NO oxidation products, we washed the catalyst after the cyclic reaction. Then, the washing liquid was taken for ion chromatography detection, and the results are shown in Table S5. Based on this result, the selectivity of NO products can be determined. As can be seen from the Fig. 5c, the selectivity of NO conversion to NO₃⁻ on Cl-Sr/Nb₂O₅ surface is greatly improved compared with Nb₂O₅.

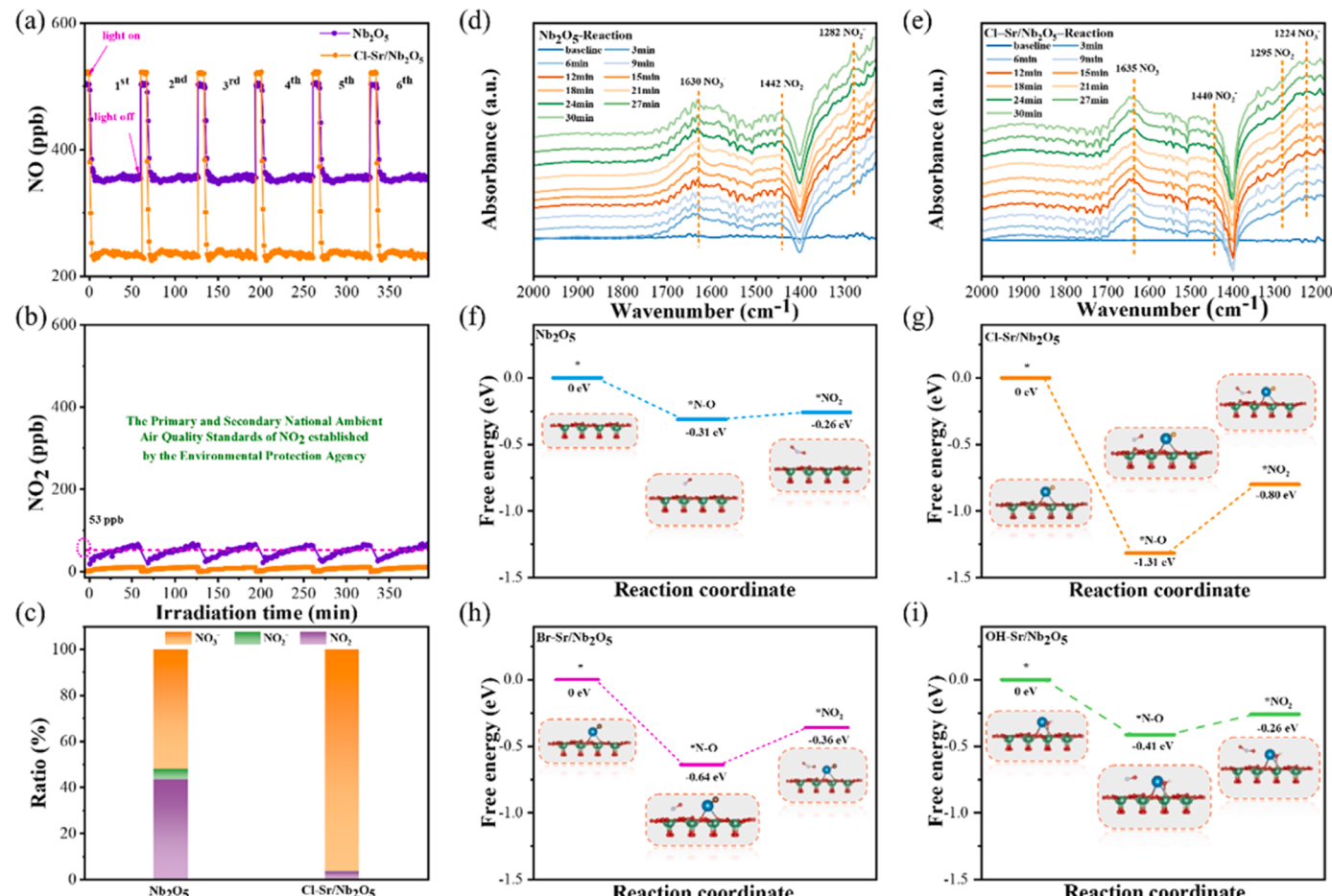


Fig. 5. (a)-(b) Multicycle photocatalytic removal of NO (500 ppb) by Nb₂O₅ and Cl-Sr/Nb₂O₅ under visible light. (c) Distribution of NO oxidation products over Nb₂O₅ and Cl-Sr/Nb₂O₅. In-situ DRIFTS spectra of Nb₂O₅ (d) and Cl-Sr/Nb₂O₅ (e) for photocatalytic NO oxidation. (f)-(i) Energy profile for *NO → *NO₂ on the Nb₂O₅, Cl-Sr/Nb₂O₅, Br-Sr/Nb₂O₅ and OH-Sr/Nb₂O₅. “*” indicates the surface adsorption state. The green, red, blue, orange, brown and pink spheres represent Nb, O, Sr, Cl, Br, and H atoms, respectively.

In order to examine the photocatalytic NO oxidation conversion process and the underlying reaction mechanism, the reaction intermediates were monitored by the use of in-situ DRIFTS, and the obtained data are shown in Fig. 5d-e and S10. The peak value appears at 1224–1228 cm⁻¹ is attributed to the surface adsorption of bi-NO₃⁻ [54]. In addition, nitrite (NO₂⁻) was detected in the 1295 cm⁻¹ and 1440–1442 cm⁻¹ bands; these peaks are partial oxidation products of nitric oxide [17,55]. Compared with the other three catalysts, Cl-Sr/Nb₂O₅ catalyst exhibits the highest bi-NO₃⁻ (1224 cm⁻¹) signal intensity and the weakest NO₂⁻ signal intensity. It is suggested that the introduction of Sr atom and the change of ligand can regulate the NO oxidation path.

The thermodynamics could be significantly influenced by various ligands, as indicated by the experimental findings mentioned above. DFT calculations are used to further reveal potential mechanisms of small molecule activation and transformation pathways. Since there are two reactants, NO and O₂, we first analyzed the adsorption capacity of the reactants on the catalyst surface. As shown in Fig. S11-13, the adsorption energies of NO on Nb₂O₅, Cl-Sr/Nb₂O₅, Br-Sr/Nb₂O₅ and OH-Sr/Nb₂O₅ are -0.289 eV, -1.47 eV, -1.42 eV, and -0.287 eV, indicating that NO molecules are more strongly adsorbed on Cl-Sr/Nb₂O₅. This result also shows that NO is more easily adsorbed on the catalyst surface than O₂. Based on this premise, we proceed to further examine the oxidation processes of nitrogen monoxide (NO) on the surface of the catalysts. It can be seen from Fig. 5f-i that among the four catalysts, Cl-Sr/Nb₂O₅ has the highest energy barrier (0.5 eV) during the

conversion from NO to NO_2 , indicating that $^*\text{NO}_2$ formation is significantly inhibited on Cl-Sr/Nb₂O₅. The changing trend of free energy (ΔG) for NO molecule oxidizing to NO_3^- on Nb₂O₅, Cl-Sr/Nb₂O₅, Br-Sr/Nb₂O₅ and OH-Sr/Nb₂O₅ in the presence of O₂ was further studied, as shown in Fig. S14. It is worth noting that all NO oxidation processes are exothermic except $^*\text{HNO}_3$ desorption. The optimized structures of the adsorption of $^*\text{NO}_2$ and HNO₃ on Nb₂O₅, Cl-Sr/Nb₂O₅, Br-Sr/Nb₂O₅, and OH-Sr/Nb₂O₅ are also shown in Fig. S15–16. Thus, we can conclude that NO can be strongly activated to NO⁺, and then NO⁺ can be oxidized to nitrate by an exothermic process, resulting in the storage of nitrate on the surface of the sample.

4. Conclusions

In summary, we suggest an innovative approach involving the use of a simple impregnation technique to synthesize efficient photocatalysts for NO deep oxidation. Benefiting from the ligand-induced local structure regulation, the Cl-Sr/Nb₂O₅ exhibits the highest NO oxidation photocatalytic activity, and also releases the lowest harmful intermediate NO₂. The introduction of Sr single atom and the change of ligand can regulate the oxidation path of NO. Density functional theory analysis revealed that the introduction of Sr active sites and ligand further improved the formation energy barrier of $^*\text{NO}_2$, so Cl-Sr/Nb₂O₅ catalyst could produce highly selective nitrate by inhibiting the formation of NO₂. This study offers novel perspectives on the design and synthesis of locally regulated structures in supported monatomic metals.

CRediT authorship contribution statement

Zhang Yumei: Formal analysis. **Wang Lin:** Formal analysis. **An Jing:** Methodology. **Luo Qingzhi:** Investigation, Resources. **Mu Huiying:** Software. **Duan Yandong:** Conceptualization, Formal analysis, Funding acquisition, Methodology, Resources, Supervision, Writing – original draft, Writing – review & editing. **Wang Desong:** Conceptualization, Formal analysis, Resources, Supervision. **Wu Tianjiao:** Data curation, Formal analysis, Investigation, Methodology, Writing – original draft. **Bai Huanhuan:** Data curation, Formal analysis. **Ma Bibo:** Data curation.

Declaration of Competing Interest

The authors declare that they have no known competing financial interests or personal relationships that could have appeared to influence the work reported in this paper.

Data Availability

No data was used for the research described in the article.

Acknowledgements

This work was supported by the Science and Technology Project of Hebei Education Department (ZD2022122), National Natural Science Foundation of China (No. 22278349) and Natural Science Foundation of Hebei Province (No. B2021208007). The theoretical work was carried out at Bianshui Riverside Supercomputing Center (BRSC). The authors would like to thank Haipeng Liu from shiyanjia Lab (www.shiyanjia.com) for the XPS analysis.

Appendix A. Supporting information

Supplementary data associated with this article can be found in the online version at [doi:10.1016/j.apcatb.2023.123688](https://doi.org/10.1016/j.apcatb.2023.123688).

References

- [1] Q. Zhu, R. Hailili, Y. Xin, Y. Zhou, Y. Huang, X. Pang, K. Zhang, P.K.J. Robertson, D.W. Bahnemann, C. Wang, *Appl. Catal. B: Environ.* 319 (2022) 121888.
- [2] H. Shang, M. Li, H. Li, S. Huang, C. Mao, Z. Ai, L. Zhang, *Environ. Sci. Technol.* 53 (2019) 6444–6453.
- [3] Y. Lu, M. Chen, L. Jiang, J. Cao, H. Li, S.C. Lee, Y. Huang, *Environ. Chem. Lett.* 20 (2022) 3905–3925.
- [4] Z. Li, Q. Zhou, J. Liang, L. Zhang, X. Fan, D. Zhao, Z. Cai, J. Li, D. Zheng, X. He, Y. Luo, Y. Wang, B. Ying, H. Yan, S. Sun, J. Zhang, A.A. Alshehri, F. Gong, Y. Zheng, X. Sun, *Small* 19 (2023) 2300291.
- [5] B. Yuan, Z. Qian, X. Yang, M. Luo, X. Feng, L. Fu, W. Yang, L. Yang, J. Zhang, Y. Zhao, R. Hao, *Environ. Sci. Technol.* 56 (2022) 10423–10432.
- [6] Y. Zeng, K. Haw, Y. Wang, S. Zhang, Z. Wang, Q. Zhong, S. Kawi, *ChemCatChem* 13 (2021) 491–505.
- [7] N. Li, C. Wang, K. Zhang, H. Lv, M. Yuan, D.W. Bahnemann, *Chin. J. Catal.* 43 (9) (2022) 2363–2387.
- [8] J. Liao, K. Li, H. Ma, F. Dong, X. Zeng, Y. Sun, *Chin. Chem. Lett.* 31 (2020) 2737–2741.
- [9] A. Fujishima, K. Honda, *Nature* 238 (1972) 37–38.
- [10] G. Liu, Y. Huang, H. Lv, H. Wang, Y. Zeng, M. Yuan, Q. Meng, C. Wang, *Appl. Catal. B: Environ.* 284 (2021) 119683.
- [11] J. Zhang, Z. Li, B. Liu, M. Chen, Y. Zhou, M. Zhu, *Appl. Catal. B: Environ.* 328 (2023) 122522.
- [12] Z. Gu, Z. Cui, Z. Wang, K.S. Qin, Y. Asakura, T. Hasegawa, S. Tsukuda, K. Hongo, R. Maezono, S. Yin, *Appl. Catal. B: Environ.* 279 (2020) 119376.
- [13] G. Cheng, X. Liu, X. Song, X. Chen, W. Dai, R. Yuan, X. Fu, *Appl. Catal. B: Environ.* 277 (2020) 119196.
- [14] X. Shen, G. Dong, L. Wang, L. Ye, J. Sun, *Adv. Mater. Interfaces* 6 (2019) 1901032.
- [15] Z. Chen, H. Yin, C. Wang, R. Wang, Y. Peng, C. You, J. Li, *Environ. Sci. Technol.* 55 (2021) 9285–9292.
- [16] F. Rao, G. Zhu, W. Zhang, Y. Xu, B. Cao, X. Shi, J. Gao, Y. Huang, Y. Huang, M. Hojaberdiiev, *ACS Catal.* 11 (2021) 7735–7749.
- [17] P. Chen, H. Liu, Y. Sun, J. Li, W. Cui, L. Wang, W. Zhang, X. Yuan, Z. Wang, Y. Zhang, F. Dong, *Appl. Catal. B: Environ.* 264 (2020) 118545.
- [18] N. Li, C. Wang, K. Zhang, H. Lv, M. Yuan, D.W. Bahnemann, *Chin. J. Catal.* 43 (2022) 2363–2387.
- [19] B. Qiao, A. Wang, X. Yang, L.F. Allard, Z. Jiang, Y. Cui, J. Liu, J. Li, T. Zhang, *Nat. Chem.* 3 (2011) 634–641.
- [20] H. Xu, Z. Zhang, J. Liu, C.-L. Do-Thanh, H. Chen, S. Xu, Q. Lin, Y. Jiao, J. Wang, Y. Wang, Y. Chen, S. Dai, *Nat. Commun.* 11 (2020), 3908.
- [21] W. Guo, Z. Wang, X. Wang, Y. Wu, *Adv. Mater.* 33 (2021) 2004287.
- [22] J. Li, Q. Guan, H. Wu, W. Liu, Y. Lin, Z. Sun, X. Ye, X. Zheng, H. Pan, J. Zhu, S. Chen, W. Zhang, S. Wei, J. Lu, *J. Am. Chem. Soc.* 141 (2019) 14515–14519.
- [23] J. Liu, Y. Wang, J. Li, *J. Am. Chem. Soc.* 139 (2017) 6190–6199.
- [24] J. Wu, Y. Wu, L. Lu, D. Zhang, X. Wang, *Talanta Open* 4 (2021) 100075.
- [25] Y. Li, Y. Wang, G. Cui, T. Zhu, J. Zhang, C. Yu, J. Cui, J. Wu, H.H. Tan, Y. Zhang, Y. Wu, *ACS Appl. Energy Mater.* 3 (2020) 12037–12045.
- [26] J. Yan, G. Wu, N. Guan, L. Li, *Appl. Catal. B: Environ.* 152–153 (2014) 280–288.
- [27] Y. Wang, X. Hu, H. Song, Y. Cai, Z. Li, D. Zu, P. Zhang, D. Chong, N. Gao, Y. Shen, C. Li, *Appl. Catal. B: Environ.* 299 (2021) 120677.
- [28] S. Li, M. Dong, J. Yang, X. Cheng, X. Shen, S. Liu, Z. Wang, X. Gong, H. Liu, B. Han, *Nat. Commun.* 12 (2021) 584.
- [29] J. Xu, H. Xu, A. Dong, H. Zhang, Y. Zhou, H. Dong, B. Tang, Y. Liu, L. Zhang, X. Liu, J. Luo, L. Bie, S. Dai, Y. Wang, X. Sun, Y. Li, *Adv. Mater.* 34 (2022) 2206991.
- [30] Z. Li, H. Li, Z. Yang, X. Lu, S. Ji, M. Zhang, J.H. Horton, H. Ding, Q. Xu, J. Zhu, J. Yu, *Small* 18 (2022) 2201092.
- [31] J. Liu, C. Cao, X. Liu, L. Zheng, X. Yu, Q. Zhang, L. Gu, R. Qi, W. Song, *Angew. Chem. Int. Ed.* 60 (2021) 15248–15253.
- [32] B. Hu, K. Sun, Z. Zhuang, Z. Chen, S. Liu, W. Cheong, C. Chen, M. Hu, X. Cao, J. Ma, R. Tu, X. Zheng, H. Xiao, X. Chen, Y. Cui, Q. Peng, C. Chen, Y. Li, *Adv. Mater.* 34 (2022) 2107721.
- [33] T. Zhang, J. Jin, J. Chen, Y. Fang, X. Han, J. Chen, Y. Li, Y. Wang, J. Liu, L. Wang, *Nat. Commun.* 13 (2022) 6875.
- [34] P. Liu, Z. Huang, X. Gao, X. Hong, J. Zhu, G. Wang, Y. Wu, J. Zeng, X. Zheng, *Adv. Mater.* 34 (2022) 2200057.
- [35] G. Kresse, D. Joubert, *Phys. Rev. B* 59 (1999) 1758–1775.
- [36] G. Kresse, J. Furthmüller, *Phys. Rev. B* 54 (1996) 11169–11186.
- [37] G. Kresse, J. Furthmüller, *Comput. Mater. Sci.* 6 (1996) 15–50.
- [38] J.P. Perdew, K. Burke, M. Ernzerhof, *Phys. Rev. Lett.* 77 (1996) 3865–3868.
- [39] D. Chen, J. Wang, T. Chou, B. Zhao, M.A. El-Sayed, M. Liu, *J. Am. Chem. Soc.* 139 (2017) 7071–7081.
- [40] J. Xu, Y. Wang, K. Wang, M. Zhao, R. Zhang, W. Cui, L. Liu, M.S. Bootharaju, J. H. Kim, T. Hyeon, H. Zhang, Y. Wang, S. Song, X. Wang, *Angew. Chem. Int. Ed.* 62 (2023) e202302877.
- [41] R. Bhardwaj, A. Hazra, *ACS Appl. Nano Mater.* 5 (2022) 15507–15517.
- [42] A. Hazra, R. Bhardwaj, *ACS Appl. Electron. Mater.* 5 (2023) 265–274.
- [43] X. Wang, Q. Li, L. Zhang, Z. Hu, L. Yu, T. Jiang, C. Lu, C. Yan, J. Sun, Z. Liu, *Adv. Mater.* 30 (2018) 1800963.
- [44] Z. Pei, H. Guo, L. Zhu, C. Li, Z. Fu, J. Xu, *Mater. Sci. Eng. B* 287 (2023) 116134.
- [45] X. Yuan, S. Tang, S. Qiu, X. Liu, *J. Phys. Chem. C.* 127 (2023) 1828–1840.
- [46] X. Wang, S. Li, Z. Yuan, Y. Sun, Z. Tang, X. Gao, H. Zhang, J. Li, S. Wang, D. Yang, J. Xie, Z. Yang, Y. Yan, *Angew. Chem.* 135 (2023) e202303794.
- [47] X. Jiang, Q. Gao, X. Xu, G. Xu, D. Li, B. Cui, D. Liu, F. Qu, *Phys. Chem. Chem. Phys.* 23 (2021) 21641–21651.

[48] Z. Liu, C. Zhang, L. Liu, T. Zhang, J. Wang, R. Wang, T. Du, C. Yang, L. Zhang, L. Xie, W. Zhu, T. Yue, J. Wang, *Adv. Mater.* 33 (2021) 2104099.

[49] X. Gao, Y. Shen, J. Liu, L. Lv, M. Zhou, Z. Zhou, Y. Ping Feng, L. Shen, *Appl. Surf. Sci.* 599 (2022) 153942.

[50] H. Li, H. Ji, J. Liu, W. Liu, F. Li, Z. Shen, *Appl. Catal. B: Environ.* 328 (2023) 122481.

[51] F. Guo, H. Zhang, H. Li, Z. Shen, *Appl. Catal. B: Environ.* 306 (2022) 121092.

[52] Z. Chen, H. Yin, R. Wang, Y. Peng, C. You, J. Li, *Environ. Sci. Technol.* 56 (2022) 3604–3612.

[53] H. Li, H. Zhu, Y. Shi, H. Shang, L. Zhang, J. Wang, *Environ. Sci. Technol.* 56 (2022) 1771–1779.

[54] P. Chen, F. Dong, M. Ran, J. Li, *Chin. J. Catal.* 39 (2018) 619–629.

[55] Z. Guo, W. Huo, T. Cao, F. Fan, G. Ge, X. Liu, K. Chen, H. Yao, F. Dong, Y. Zhang, *CrystEngComm* 22 (2020) 257–266.